Available online at www.sciencedirect.com
ScienceDirect
International Journal of Heat and Mass Transfer 51 (2008) 960–968
International Journal of HEAT and MASS TRANSFER
www.elsevier.com/locate/ijhmt

Technical Note

Computation of buoyancy-induced flow in a heated rotating cavity with an axial throughflow of cooling air

Shuqing Tian *, Zhi Tao, Shuiting Ding, Guoqiang Xu

National Key Laboratory on Aero-Engines, School of Jet Propulsion, Beijing University of Aeronautics and Astronautics, Beijing 100083, PR China

Received 20 January 2007; received in revised form 21 September 2007

Abstract

In the cavity between the co-rotating compressor discs in gas turbine engines, the flow is very complex because of the multiple driving forces including the centrifugal buoyancy force, the Coriolis force and the inertial force. Numerical analysis was carried out in a simple rotating cavity with cooling air axial throughflow and a heated shroud. Efforts were focused upon the flow structure and its variations. The results reveal the non-axisymmetrical flow structures with cyclonic and anti-cyclonic circulations, which slip relative to the rotating cavity in the opposite direction (that is, rotate with a slower speed than the cavity) and the patterns remain unchanged. These structures are not unique, and four types with one, two, three, four pairs of circulations are obtained. For any particular set of conditions, the final structure can depend on the path taken: as axial Reynolds number is increased the number of circulation couples increases, and as Grashof number is increased the number of circulation couples decreases. At high Grashof number, the variation of Nu_{av} with Gr is consistent with the Rayleigh–Bénard convection.

Keywords: Rotating cavity; Buoyancy force; Free convection; Instability

1. Introduction

In modern gas-turbine aero engines, cooling air extracted from the compressor is ducted through rotating cylindrical cavities to cool certain engine components. It is important for the engine designer to get an accurate knowledge of the flow and heat transfer behaviour in these cavities to further improve the engine efficiency. A simplified high-compressor drum is shown in Fig. 1, which comprises two pierced discs and a cylindrical shroud. All the surfaces of the cavity rotate with an angular velocity Ω, and an axial throughflow of cooling air enters and exits the cavity through the center holes of the discs.

The buoyancy-affected flow in this rotating cavity is known to be complex. Previous experiments and numerical tests found large-scale instabilities although the boundary conditions are stable. Farthing et al. [1] conducted flow visualization experiments and found that the flow patterns in the rotating cavity with heated discs were non-axisymmetric and time-dependent. There were one pair of cyclonic and anti-cyclonic circulations in the axial mid-plane, as shown in Fig. 2. Between theses circulations were the dead zone and the "radial arm". Cooling air invaded the cavity through the "radial arm" towards the rim. The rotational speed of the whole flow structure was slower than that of the cavity.

Tian et al. [2] numerically investigated the flow and heat transfer in a rotating cavity with a heated shroud based on the geometry of Farthing et al. [1]. Their 3D, steady, turbulent computations showed that the flow in the cavity comprised two parts: the Rayleigh-Bénard convection in the larger radius region, and the forced convection in the central region. There was a critical Rayleigh number above which the flow becomes unsteady and time-dependent. The centrifugal buoyancy force was found to be the key factor leading to flow instability.

* Corresponding author.
E-mail address: sq_tian@hotmail.com (S. Tian).

0017-9310/$ - see front matter © 2007 Elsevier Ltd. All rights reserved.
doi:10.1016/j.ijheatmasstransfer.2007.09.040

Nomenclature

a	inner radius of cavity
b	outer radius of cavity
Bo	Buoyancy parameter, $Gr/(Re_z)^2 = \beta\Delta T Re_\phi^2/Re_z^2$
C_p	specific heat capacity
G	gap ratio, s/b
Gr	Grashof number, $\beta\Delta T Re_\phi^2$
n	iteration step
N	number of circulation pairs in cavity
Nu	Nusselt number, $qb/\lambda\Delta T$
P	pressure
Pr	Prandtl number
q	heat flux
r, θ, z	radial, tangential and axial coordinates, respectively
Ra	Rayleigh number, $Pr \cdot Gr$
Re_z	axial Reynolds number, Wa/v
Re_ϕ	rotational Reynolds number, $\Omega b^2/v$
s	axial distance between discs
T	temperature
T_0	inlet air temperature
T_{sh}	shroud temperature
u, v, w	radial, tangential and axial velocities, respectively
U_τ	friction velocity, $\sqrt{\tau_w/\rho}$
W	axial inlet velocity
X	dimensionless radial coordinate, r/b
y	generalized wall distance
y^+	wall distance Reynolds number, yU_τ/v
Z	dimensionless axial coordinate, z/s

Greek symbols

ΔT	temperature difference, $T_{sh} - T_0$
Ω	angular speed of cavity
β	thermal expansion coefficient, $1/T_0$
λ	thermal conductivity
μ	dynamic viscosity
v	kinematic viscosity
ρ_0	characteristic density
τ_w	total shear stress at the wall

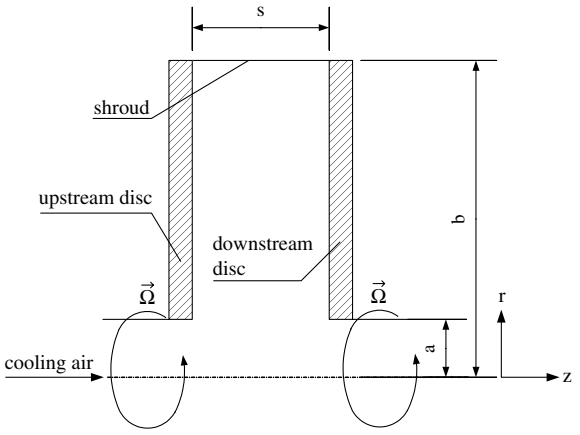

Fig. 1. Rotating cavity with an axial throughflow of cooling air.

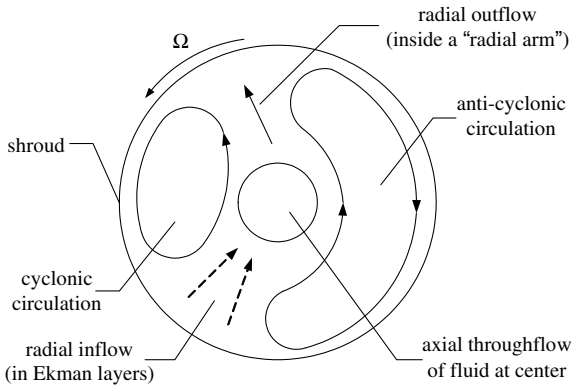

Fig. 2. Schematic of flow structure [1].

Tucker and Long [3,4] carried out time-dependent compressible CFD calculations for the rotating cavity. They obtained a reasonable qualitative agreement with flow visualization observed by Farthing et al. [1]. They found that the flow structures were significantly influenced by the cavity surface temperature distributions, and the instability was caused by vortex breakdown.

Sun et al. [5] conducted numerical investigations on the buoyancy-affected flow in the rotating cavity. Their LES (large eddy simulation) and RANS (Reynolds-average Navier–Stokes) computations both confirmed the three-dimensional, unsteady flow, and suggested that the LES can achieve better agreement with flow and heat transfer measurements than RANS model.

Long et al. [6,7] carried out a combined computational and experimental study for this heated rotating flow, and found that some of the axial throughflow invaded the region near the rim of the cavity, cyclonic and anti-cyclonic circulations were observed near the heated shroud. The cause of the instability was concluded to be the rotationally induced buoyancy forces.

Bohn et al. [8,9] conducted experimental and numerical studies on the rotating cavity with both discs heated and obtained the similar results to those of Long et al. [6,7]. The large-scale unsteady flow phenomenon was confirmed. A flow pattern changing between single pair and multi-pairs of vortices was found.

Owen et al. [10–12] performed experimental and numerical investigations on the Buoyancy-induced flow in a rotating cavity with one heated disc. The analysis also revealed a three-dimensional unsteady flow with multi-cell flow structure thought to comprise one, two or three pairs of vortices.

These flows display the characteristics of self-organizing systems, which are associated with the maximum entropy production (MEP) principle. The most probable macrostates corresponds to the maximum sum of the heat and work transfer to the system.

King et al. [13,14] numerically studied the Buoyancy-induced flow and heat transfer in a sealed rotating annulus with a heated outer cylinder and a cooled inner cylinder. Cyclonic and anti-cyclonic circulations in the r–θ plane were also captured, and the computed Nusselt numbers increase with the Rayleigh number in agreement with correlations for Rayleigh–Bénard convection in a stationary enclosure [15].

In summary, it can be seen that the flow in the heated rotating cavities is very complex because of the multiple driving forces including the buoyancy force, the Coriolis force and the inertial force. This paper analyzed the effects of the forces on the flow structures by using numerical simulations. Efforts were focused upon the buoyancy-induced flow structure and its variations. The investigated cavity has a heated shroud and the cooling air passes through the centers as shown in Fig. 1.

2. Numerical algorithm

The investigated geometry is shown in Fig. 1, $a = 40$ mm, $b = 175$ mm and $s = 40$ mm giving a gap ratio $G = s/b$ of 0.229. The corresponding computational grid had a total of 145,728 cells, with 2024 in the r–z plane and 72 in the tangential direction. The grid spacing near surfaces is refined using geometric expansions, and the closest off-wall node spacing is maintained at $y^+ < 0.5$. Sensible grid independence of the solutions has been verified by comparison with predictions obtained on a grid with 30, 45, 30 percent more nodes in the radial, tangential and axial, respectively.

The 3D steady incompressible CFD simulations were computed in the rotating frame fixed on the discs. The density variation in centrifugal force is stated by Boussinesq hypothesis, and its variations in other items are ignored. In this investigation, the centrifugal acceleration is of several orders of magnitude greater than the gravitational acceleration, and so the latter is neglected. The steady momentum equation and energy equation are given by the following equations:

$$\rho_0(\vec{V}\cdot\nabla)\vec{V} = -\nabla p_{\text{eff}} + \mu\nabla^2\vec{V} - 2\rho_0\vec{\Omega}\times\vec{V} + \rho_0\beta(T-T_0)\vec{\Omega}\times\vec{\Omega}\times\vec{r} \quad (1)$$

$$\rho_0 C_P(\vec{V}\cdot\nabla T) = \lambda\nabla^2 T \quad (2)$$

The centrifugal force is a conservative force and often put in the pressure item, and so in Eq. (1), $p_{\text{eff}} = p - \rho_0\Omega^2 r^2/2$, the symbol β is the thermal expansion coefficient, $\rho_0\beta(T-T_0)\vec{\Omega}\times\vec{\Omega}\times\vec{r}$ is the buoyancy force, $-2\rho_0\vec{\Omega}\times\vec{V}$ is the Coriolis force. The equations are solved using finite-volume (FV) method with QUICK differencing scheme, SIMPLE pressure correction algorithm.

The feasibility of the numerical algorithm that uses steady-state solvers to simulate the flow instability can be analyzed by the following facts.

In unsteady state formulation for a variable ϕ,

$$a_P\phi_P^m = \left(\sum a_{nb}\phi_{nb}^m + b\right) + a_P^0\phi_P^{m-1} \quad (3)$$

or could be rewritten as:

$$a_P^*\phi_P^m = \left(\sum a_{nb}\phi_{nb}^m + b\right) - a_P^0(\phi_P^m - \phi_P^{m-1}) \quad (4)$$

m stands for the time steps, b is source item,

$$a_P = \sum a_{nb} + b + a_P^0, \quad a_P^0 = (\rho V)^0/\delta t, \quad \text{and}$$
$$a_P^* = \sum a_{nb} + b.$$

Unsteady state formulation could be used for steady cases because with $m \to \infty$, $\phi_P^m - \phi_P^{m-1} \to 0$, and Eq. (4) converts to be a pure steady-state formulation as the following.

Steady-state formulation for a variable ϕ,

$$a_P\phi_P^n = \left(\sum a_{nb}\phi_{nb}^n + b\right) \quad (5)$$

n stands for the iteration steps. Eq. (5) is always under-relaxed such that

$$\frac{a_P}{\alpha}\phi_P^n = \left(\sum a_{nb}\phi_{nb}^n + b\right) + \frac{1-\alpha}{\alpha}a_P\phi_P^{n-1} \quad (6)$$

or could be rewritten as:

$$a'_P\phi_P^n = \left(\sum a_{nb}\phi_{nb}^n + b\right) + a''_P\phi_P^{n-1} \quad (7)$$

$$a_P\phi_P^n = \left(\sum a_{nb}\phi_{nb}^n + b\right) - a''_P(\phi_P^n - \phi_P^{n-1}) \quad (8)$$

In the equations, α is relax factor, $a_P = \sum a_{nb} + b$ and $a''_P = \frac{1-\alpha}{\alpha}a_P$.

Eqs. (7) and (8) of steady-state formulation resemble Eqs. (3) and (4) in unsteady state form, respectively. n in (7) and (8) is essentially equivalent to m in (3) and (4) such that Δn stands for a certain period of time Δt. Steady solution solver is essentially equivalent to unsteady solution solver.

The low Re k–ε turbulence model was used. No-slip conditions were used on the walls. A uniform temperature was set on the shroud, and the other outside surfaces were adiabatic. As the solid walls were included in the calculation domain, the fluid and solid conjugate heat transfer calculation was used. For the inlet, a uniform velocity condition was defined, and the full-developed outlet boundary condition was defined at the outlet.

The measure employed to judge convergence is a normalized absolute residual sum of FV solution, defined as 10^{-4} for this study. The analysis was carried out in the range of the Grashof number $Gr = 2.81\times10^7$–6.89×10^9, the axial

Reynolds number $Re_z = 1.34 \times 10^4$–1.14×10^5, and the rotational Reynolds number $Re_\phi = 1.29 \times 10^4$–$1.55 \times 10^5$.

3. Numerical simulation reliability

To validate the numerical simulations, an experimental model done by Farthing [16] was employed to calculate, and the results were compared with the experiments in Fig. 3.

In the rotating cavity with cooling air axial throughflow and symmetrically heated discs, the predicted flow structures are three-dimensional with cyclonic and anti-cyclonic circulations in the axial mid-plane, which are consistent with the photographs captured in the experiments, the core of fluid slips relative to the rotating discs with iteration steps in the opposite direction, and two types of flow structures with one and two pairs of circulations are obtained. The calculated average Nusselt numbers in discs are in reasonable agreement with the experiments. The 3D steady calculation can portray the flow and heat transfer in the rotating cavity.

4. Numerical results and analysis

4.1. Fixing Re_z and $\beta\Delta T$, increasing Re_Φ

In this section, the axial Reynolds number is fixed at $Re_z = 2.686 \times 10^4$, $\beta\Delta T = 0.169$, and the rotational Reynolds number is varied from 1.29×10^4 to 1.55×10^5 (Gr is varied from 2.81×10^7 to 4.06×10^9 correspondingly). Thereby, the inertial force is held constant, the centrifugal buoyancy force and the Coriolis force are both enhanced. The influence of the rotation speed Ω on the flow structure is studied. The results are shown in Fig. 4.

Fig. 4a shows that at low rotational Reynolds number $Re_\phi = 1.29 \times 10^4$, the Buoyancy parameter $\mathrm{Bo} = 0.039$, thereby the centrifugal buoyancy force is much smaller than the inertial force, and the flow in the cavity is dominated by the forced convection and shows axisymmetrically steady. When Re_ϕ is increased to 7.73×10^4, the centrifugal buoyancy force is also increased, the flow becomes non-axisymmetrically unsteady, and three pairs of cyclonic and anti-cyclonic circulations can be observed circumferentially. And at $Re_\phi = 1.03 \times 10^5$, two circulation couples are captured. These circulations lie in the rim area of the cavity. While, as Re_ϕ is further increased to 1.55×10^5, the flow oscillation is much fiercer, one pair of circulations filling the whole cavity in radius are observed, central cooling air invades the region near the rim of the cavity through the "radial arm" between the circulations. These 3D flow structures slip relative to the cavity with iteration steps in the opposite direction of Ω and the patterns remain unchanged, which are examples of the self-organizing system (SOSs) as analyzed by Owen [12].

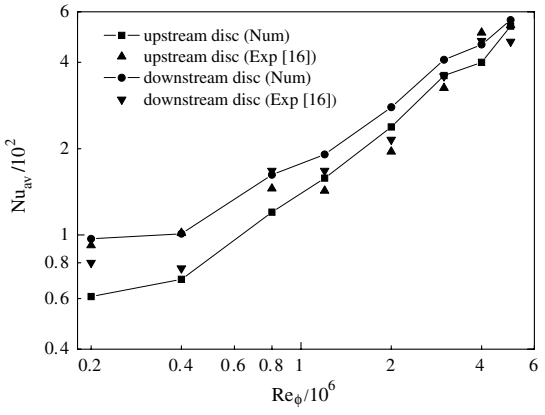

Fig. 3. Nu_{av} comparison between numerical calculation and experiments for the model [16] with heated discs for: $Re_z = 1.6 \times 10^5$.

Fig. 4b shows the velocity field in r–z plane. At low rotational Reynolds number $Re_\phi = 1.29 \times 10^4$, a powerful toroidal vortex induced by the through-passing central jet fills large region of the cavity. As Re_ϕ is increased to 7.73×10^4, the buoyancy force and the Coriolis force are enhanced, which depress the toroidal vortex to the small region near the center, and the buoyancy-induced flow fills the large upper cavity. At $Re_\phi = 1.03 \times 10^5$, the toroidal vortex becomes smaller, and the buoyancy-induced flow region expands correspondingly. While, when Re_ϕ is increased to higher value 1.55×10^5, the unsteady flow induced by the buoyancy force dominates the whole flow in the cavity, there is no obvious toroidal vortex.

Fig. 4c shows the radial distribution of velocities in $z/s = 0.5$ at different Re_ϕ. The velocities are the average values in circle at the last iteration step, which were found to agree well with iteration averages. It is obvious that in the toroidal vortex region ($0.29 < X < 0.48$) the radial velocity at $Re_\phi = 7.73 \times 10^4$ is larger than that at $Re_\phi = 1.03 \times 10^5$; in the buoyancy-induced flow region ($X > 0.48$) the tangential velocity at $Re_\phi = 7.73 \times 10^4$ is smaller than that at $Re_\phi = 1.03 \times 10^5$; the tangential velocities are positive in low radius region, and are negative in high radius region.

Fig. 5 shows the variation of the average Nusselt numbers Nu_{av} versus Grashof number Gr for this case of gap ration $G = 0.229$ with the range of $2.13 \times 10^9 < Gr < 6.89 \times 10^9$. The computed Nu_{av} represents the heat transfer of the last iteration step, which was found to agree well with iteration averages. A scaling law $Nu = C \cdot Gr^\gamma$ is used to correlate Nusselt number and Grashof number. It can be seen that at this 'high' Grashof numbers, $\gamma = 0.296$, which is in good agreement with the value 1/3 obtained by Long et al. [6] for the case of gap ration $G = 0.13$, and is also consistent with the Rayleigh–Bénard convection [17–19]. That is, in this range of 'high' Grashof number, the flow in the cavity is the Rayleigh–Bénard convection induced by the centrifugal buoyancy force.

In conclusions, in this heated rotating cavity with cooling air axial through flow, the free convection induced by the centrifugal buoyancy force and the forced convection are both existed. As Re_ϕ is increased, the free convection enhances, and the forced convection is suppressed; the flow

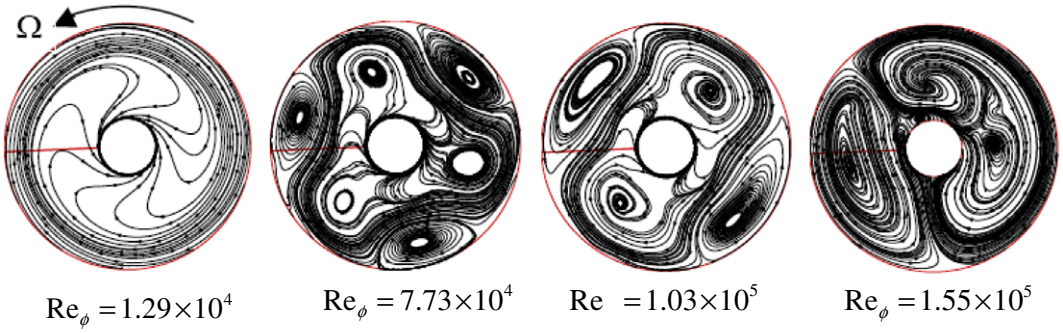

(a) Streamlines in r-θ (z/s=0.5) plane

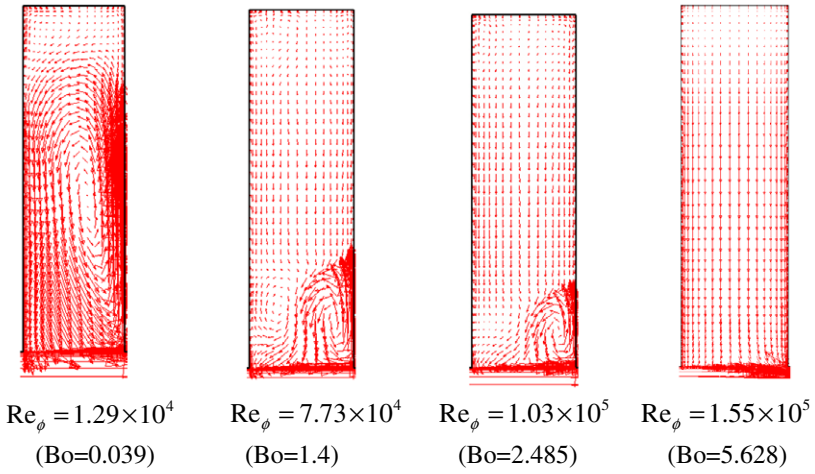

(b) Centripetal flow in r-z plane

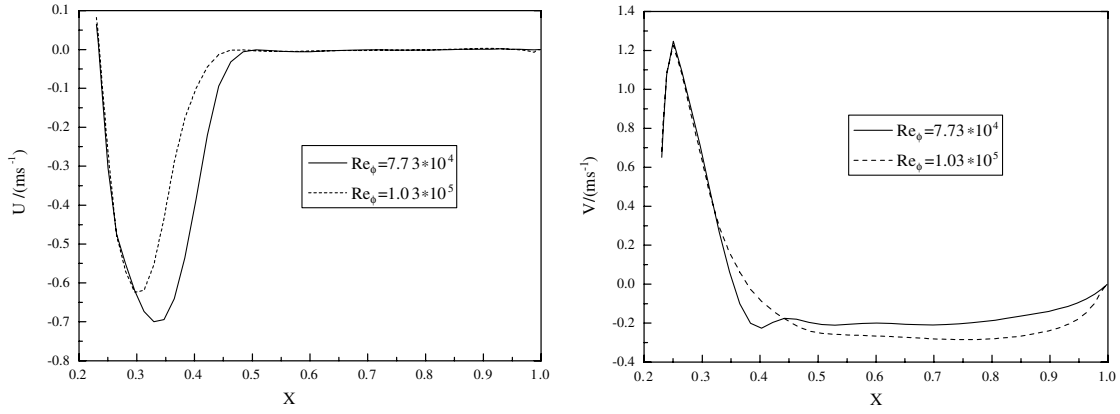

(c) Radial distributions of velocities in z/s=0.5

Fig. 4. Numerical results at different Re_ϕ for: $Re_z = 2.686 \times 10^4$, $\beta\Delta T = 0.169$.

oscillation caused by the free convection becomes fierce; and the 3D multi-cell flow structures with one, two and three circulation couples are obtained. The number of circulation couples decreases as Re_ϕ is increased.

4.2. Fixing Re_z and Re_ϕ, increasing Gr

In this section, the axial Reynolds number and the rotational Reynolds number are fixed at $Re_z = 2.686 \times 10^4$ and $Re_\phi = 1.03 \times 10^5$ separately, so the inertial force and the Coriolis force are kept constant. The temperature difference ΔT is varied from 25 to 100 °C, so the centrifugal buoyancy force enhances.

Fig. 6 shows the calculated results. It can be seen that as the Grashof number is increased, the flow oscillation becomes fierce, and the flow structure varies from two circulation couples to one couple. At $Gr = 9.104 \times 10^8$ and $Gr = 1.799 \times 10^9$, the two circulation couples lie in the

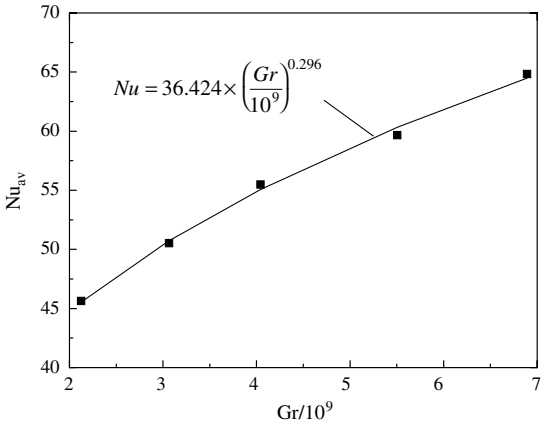

Fig. 5. Variation of average Nusselt numbers with Gr for: $Re_z = 2.686 \times 10^4$, $\beta\Delta T = 0.169$.

rim area of the cavity, which is the free convection zone, under it is the forced convection zone. As Gr is increased to 2.731×10^9, the cyclonic and anti-cyclonic circulations expand in radial direction to the whole cavity, the free convection dominates the flow in the cavity, and the central cooling air invades the rim area of the cavity through the "radial arm". As Gr is further increased to 3.641×10^9, the cyclonic circulation shrinks, and the anti-cyclonic circulation expands. The centrifugal buoyancy force is analyzed to be the key factor leading to instability.

4.3. Fixing Re_z and Gr, increasing Re_ϕ

In this section, the axial Reynolds number and the Grashof number are fixed at $Re_z = 2.686 \times 10^4$ and $Gr = 2.048 \times 10^9$ separately, so the inertial force and the centrifugal buoyancy force are held constant. The rotational Reynolds number is varied from 7.73×10^4 to 1.55×10^5, so the Coriolis force enhances. (It should be noted that the rotational Reynolds number and the temperature difference ΔT are varied simultaneously to keep constant Gr because Gr depends on Re_ϕ.)

The numerical results illustrated in Fig. 7 shows that at low rotational Reynolds number $Re_\phi = 7.73 \times 10^4$, there are two pairs of circulations filling the free convection zone; when Re_ϕ is increased to 1.03×10^5, the circulation couples decrease to one pair occupying the whole radius, the free convection dominates the flow in the cavity, cooling air invades the shroud area, and the flow oscillation becomes fiercer. While at larger rotational Reynolds number $Re_\phi = 1.29 \times 10^5$, the oscillation becomes weaker, and the flow structure restores to two pairs of circulations similar to the flow structure at $Re_\phi = 7.73 \times 10^4$, but the forced convection zone is smaller and the free convection zone with multi-cell is larger. At $Re_\phi = 1.55 \times 10^5$, the oscillation is enhanced again, and the number of circulations decreases to one pair similar to that at $Re_\phi = 1.03 \times 10^5$, but the anti-cyclonic circulation is larger.

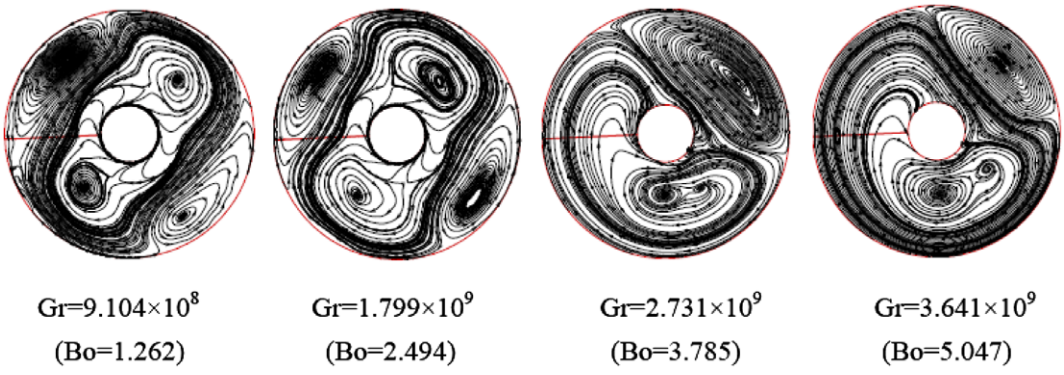

Fig. 6. Streamlines in r–θ ($z/s = 0.5$) plane for: $Re_z = 2.686 \times 10^4$, $Re_\phi = 1.03 \times 10^5$.

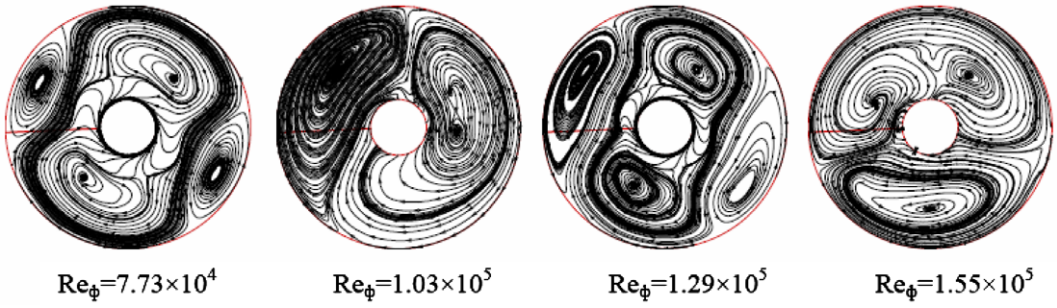

Fig. 7. Streamlines in r–θ ($z/s = 0.5$) plane for: $Re_z = 2.686 \times 10^4$, $Gr = 2.048 \times ;10^9$ (Bo = 2.839).

The above results illustrate that raising the Coriolis force without changing the centrifugal buoyancy force can not monotonously enhance the flow oscillation in the cavity.

4.4. Fixing Re_Φ and Gr, increasing Re_z

In this section, the rotational Reynolds number and the Grashof number are fixed at $Re_\phi = 1.03 \times 10^5$ and

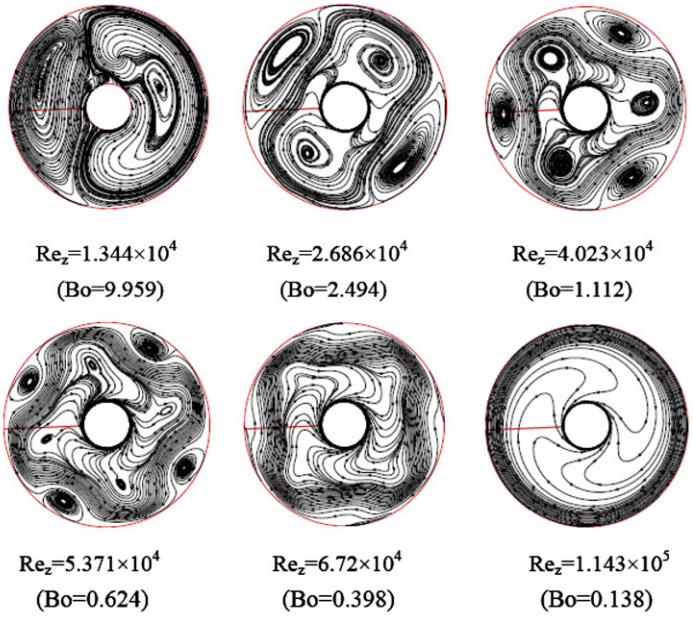

(a) Streamlines in r-θ (z/s=0.5) plane

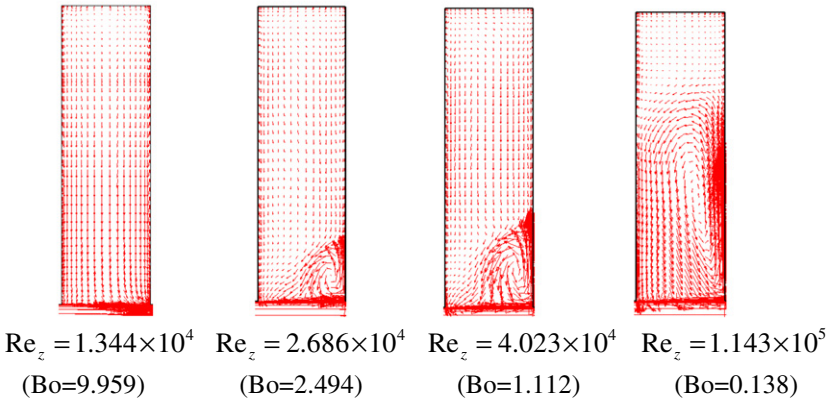

(b) Centripetal flow in r-z plane

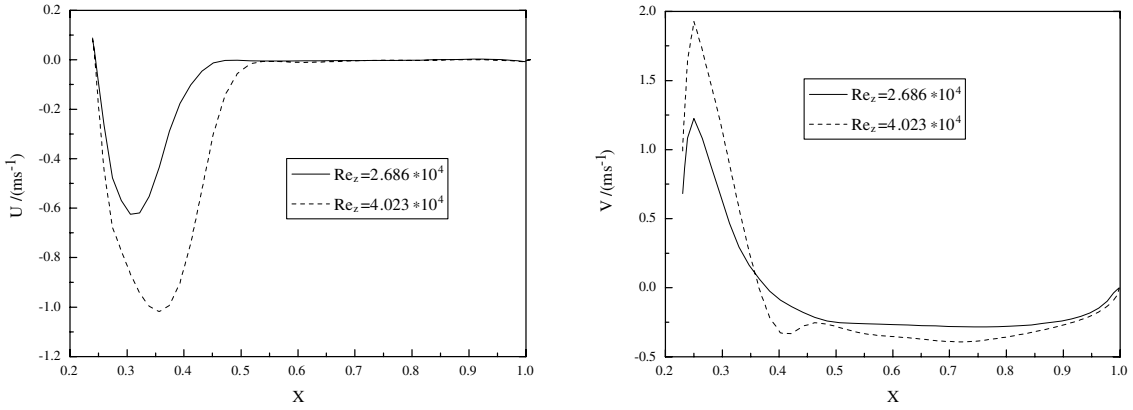

(c) Radial distributions of velocities in z/s=0.5

Fig. 8. Numerical results at different Re_z for: $Re_\phi = 1.03 \times 10^5$, $Gr = 1.799 \times 10^9$.

$Gr = 1.799 \times 10^9$ separately, so the centrifugal buoyancy force and the Coriolis force are kept constant. The axial Reynolds number is varied from 1.344×10^4 to 1.143×10^5, so the inertial force enhances. The results are illustrated in Fig. 8.

Fig. 8a shows that at low axial Reynolds number $Re_z = 1.344 \times 10^4$, the inertial force is small, and the free convection dominates the flow in the cavity, one pair of circulations extend to the whole radius, central cooling air invades and flows toward the shroud through the "radial arm". When Re_z is increased to 2.686×10^4, the forced convection enhances and dominates the flow near the center, and the free convection with two pairs of circulations is suppressed to the rim area of the cavity; the central cooling air can no longer invade the region near the shroud. As the axial Reynolds number is increased, the number of circulation couples N increases, the flow types with $N = 3$ and $N = 4$ are obtained, and the flow oscillation becomes weak. At $Re_z = 1.143 \times 10^5$ the flow has already shown axisymmetrically steady.

Fig. 8b shows the velocity field in r–z plane. The comparison of the free convection and the forced convection can be measured by the Buoyancy parameter Bo. At $\mathrm{Bo} = 9.959$, the centrifugal buoyancy force is much larger than the inertial force, and the unsteady flow induced by the free convection dominates the flow in the cavity, there is no obvious toroidal vortex caused by the forced convection. At $\mathrm{Bo} = 2.494$, the inertial force is enhanced, the superposed axial flow generates a powerful toroidal vortex near the center, and the free convection is suppressed to the upper region of the cavity. As Bo is decreased, the size of the toroidal vortex increases and the region available for buoyancy-induced flow correspondingly decreases. At $\mathrm{Bo} = 0.138$, the forced convection dominates the flow, and the toroidal vortex fills the large region of the cavity.

Fig. 8c shows the radial distribution of average velocities in circle in $z/s = 0.5$ at different Re_z. It can be seen that in the forced convection zone ($X < 0.5$) the radial velocity at $Re_z = 4.023 \times 10^4$ is larger than that at $Re_z = 2.686 \times 10^4$, and in most area of the cavity the tangential velocity at $Re_z = 4.023 \times 10^4$ is larger than that at $Re_z = 2.686 \times 10^4$.

In summary, as axial Reynolds number Re_z is increased, the flow changes from unsteady free convection to steady forced convection.

5. Conclusions

The types of flow structure in a rotating cavity with heated shroud and cooling air axial throughflow have been investigated numerically. And the 3D steady solver has been verified to be able to simulate the unsteady flow in the cavity.

The computed results reveal the non-axisymmetrical flow structures with cyclonic and anti-cyclonic circulations, as seen by previous experimenters. These structures are not unique, and four types with one, two, three, four circulation couples are captured. Moreover, these structures slip relative to the cavity with iteration steps in the opposite direction of Ω and the patterns remain unchanged. For any particular set of conditions, the final structure can depend on whether Re_ϕ, Re_z or Gr is varied.

The flow in the cavity can be divided into two typical zones: the free convection near the rim area and the forced convection near the central area. The centrifugal buoyancy force is analyzed to be the key factor leading to instability. And the enhanced inertial force can suppress the oscillation.

As Re_ϕ and Gr are increased, the number of circulation couples N decreases, the free convection enhances, and the forced convection is suppressed. While, as Re_z is increased, the process is just reverse, the number of circulation couples N increases, the forced convection enhances, and the free convection is suppressed.

At high Grashof number, the variation of Nu_{av} with Gr is consistent with the Rayleigh–Bénard convection.

Acknowledgements

We wish to thank Prof. D. Bohn who gave some support and helpful suggestions, and we also thank the reviewers for their constructive comments.

References

[1] P.R. Farthing, C.A. Long, J.M. Owen, J.R. Pincombe, Rotating cavity with axial throughflow of cooling air: flow structure, ASME J. Turbomach. 114 (1992) 237–246.
[2] S. Tian, Z. Tao, S. Ding, G. Xu, Investigation of flow and heat transfer in a rotating cavity with axial throughflow of cooling air, in: Proceedings of ASME Turbo Expo 2004, GT2004-53525, 2004.
[3] P.G. Tucker, C.A. Long, Numerical investigation into influence of geometry on flow in a rotating cavity with an axial throughflow, Int. Commun. Heat Mass Transfer 23 (3) (1996) 335–344.
[4] P.G. Tucker, C.A. Long, CFD prediction of vortex breakdown in a rotating cavity with an axial throughflow of air, Int. Commun. Heat Mass Transfer 22 (5) (1995) 639–648.
[5] Z. Sun, K. Lindblad, W. Chew, C. Young, LES and RANS investigations into buoyancy-affected convection in a rotating cavity with a central axial throughflow, in: Proceedings of ASME Turbo Expo 2006, GT2006-90251, 2006.
[6] C.A. Long, P.G. Tucker, Shroud heat transfer measurements from a rotating cavity an axial throughflow of air, ASME J. Turbomach. 116 (1994) 525–534.
[7] C.A. Long, A.P. Morse, P.G. Tucker, Measurements and computation of heat transfer in high pressure drum geometries with axial throughflow, ASME J. Turbomach. 119 (1997) 51–60.
[8] D.E. Bohn, G.N. Deutsch, B. Simon, C. Burkhardt, Flow visualization in a rotating cavity with axial throughflow, in: Proceedings of ASME Turbo Expo 2000, 2000-GT-280, 2000.
[9] D.E. Bohn, J. Ren, C. Tuemmers, Investigation of the unstable flow structure in a rotating cavity, in: Proceedings of ASME Turbo Expo 2006, GT2006-90494, 2006.
[10] J.M. Owen, Powell Jonathan, Buoyancy-induced flow in a heated rotating cavity [A], in: Proceedings of ASME Turbo Expo 2004, GT2004-53210, 2004.
[11] J.M. Owen, H. Abrahamsson, K. Lindblad, Buoyancy-induced flow in open rotating cavities, in: Proceedings of ASME Turbo Expo 2006, GT2006-91134, 2006.

[12] J.M. Owen, Thermodynamic analysis of buoyancy-induced flow in rotating cavities, in: Proceedings of ASME Turbo Expo 2007, GT 2007-27387, 2007.
[13] M.P. King, M. Wilson, J.M. Owen, Rayleig–Bénard convection in open and closed rotating cavities, in: Proceedings of ASME Turbo Expo 2005, GT 2005-68948, 2005.
[14] M.P. King, M. Wilson, Numerical simulations of convection heat transfer in Rayleig–Bénard convection and a rotating annulus, Numer. Heat Transfer. Part A: Appl. 48 (6) (2005) 529–545.
[15] K.G.T. Hollands, Multi-Prandtl number correlation equations for natural convection in layers and enclosures, Int. J. Heat Mass Transfer 27 (3) (1984) 466–468.
[16] P.R. Farthing, C.A. Long, J.M. Owen, J.R. Pincombe, Rotating cavity with axial throughflow of cooling air: heat transfer, ASME J. Turbomach. 114 (1992) 229–236.
[17] J.J. Niemela, L. Skrbek, K.R. Screenivasan, R.J. Donnelly, Turbulent convection at very high Rayleigh numbers, Nature 404 (2000) 837–840.
[18] S. Grossmann, D. Lohse, Scaling in thermal convection: a unifying theory, J. Fluid Mech. 407 (2000) 27–56.
[19] B. Castaing, G. Gunaratne, F. Heslot, L. Kadanoff, A. Libchaber, S. Thomae, X.-Z. Wu, S. Zaleski, G. Zanetti, Scaling of hard thermal turbulence in Rayleig–Bénard convection, J. Fluid Mech. 204 (1989) 1–30.